

## Correlation between the whole small recess offset and electrical performance of InP-based HEMTs

GONG Hang<sup>1,2</sup>, ZHOU Fu-Gui<sup>1,2</sup>, FENG Ruize<sup>1,2</sup>, FENG Zhi-Yu<sup>1,2</sup>, LIU Tong<sup>1</sup>, SHI Jing-Yuan<sup>1,2</sup>,  
SU Yong-Bo<sup>1,2\*</sup>, JIN Zhi<sup>1,2\*</sup>

1. High-Frequency High-Voltage Device and Integrated Circuits Center, Institute of Microelectronics, Chinese Academy of Sciences, Beijing 100029, China;
2. University of Chinese Academy of Sciences (UCAS), Beijing 100049, China)

**Abstract:** In this work, we investigate the impact of the whole small recess offset on DC and RF characteristics of InP high electron mobility transistors (HEMTs).  $L_g = 80$  nm HEMTs are fabricated with a double-recessed gate process. We focus on their DC and RF responses, including the maximum transconductance ( $g_{m,max}$ ), ON-resistance ( $R_{ON}$ ), current-gain cutoff frequency ( $f_T$ ), and maximum oscillation frequency ( $f_{max}$ ). The devices have almost same  $R_{ON}$ . The  $g_{m,max}$  improves as the whole small recess moves toward the source. However, a small gate to source capacitance ( $C_{gs}$ ) and a small drain output conductance ( $g_{ds}$ ) lead to the largest  $f_T$ , although the whole small gate recess moves toward the drain leads to the smaller  $g_{m,max}$ . According to the small-signal modeling, the device with the whole small recess toward drain exhibits an excellent RF characteristics, such as  $f_T = 372$  GHz and  $f_{max} = 394$  GHz. This result is achieved by paying attention to adjust resistive and capacitive parasitics, which play a key role in high-frequency response.

**Key words:** InP high-electron-mobility transistor (InP HEMT), InGaAs/InAlAs, DC/RF characteristic, small-signal modeling, double-recessed gate process

## InP 基 HEMT 的整体小凹槽偏移与电学性能的相关性

龚航<sup>1,2</sup>, 周福贵<sup>1,2</sup>, 封瑞泽<sup>1,2</sup>, 冯识谕<sup>1,2</sup>, 刘桐<sup>1</sup>, 史敬元<sup>1,2</sup>, 苏永波<sup>\*1,2</sup>, 金智<sup>1,2</sup>

1. 中国科学院微电子研究所, 高频高压器件与集成电路研究中心, 北京 100029;
2. 中国科学院大学, 北京 100049)

**摘要:**在这项工作中,我们研究了整个小凹槽偏移对 InP 高电子迁移率晶体管(HEMT)的直流和射频特性的影响。 $L_g=80$  nm HEMT 采用双凹栅极工艺制造。我们重点关注它们的直流和射频响应,包括最大跨导( $g_{m,max}$ )、导通电阻( $R_{ON}$ )、电流增益截止频率( $f_T$ )和最大振荡频率( $f_{max}$ )。这些设备具有几乎相同的 $R_{ON}$ 。随着整个小凹槽向源移动, $g_{m,max}$ 会提高。然而,尽管整个小栅极凹槽向漏极移动会导致较小 $g_{m,max}$ ,但较小的栅源电容( $C_{gs}$ )和较小的漏极输出电导( $g_{ds}$ )会导致最大的 $f_T$ 。根据小信号建模,整个小凹槽朝向漏极的器件表现出优异的射频特性,例如 $f_T=372$  GHz和 $f_{max}=394$  GHz。这一结果是通过注意调整电阻和电容寄生效应来实现的,这些寄生效应在高频响应中起着关键作用。

**关键词:**InP 高电子迁移率晶体管(InP HEMT); InGaAs/InAlAs; DC/RF 特性; 小信号建模; 双凹栅工艺  
**中图分类号:** TN385 **文献标识码:** A

Received date: 2024-03-05, revised date: 2024-08-05

收稿日期: 2024-03-05, 修回日期: 2024-08-05

Foundation item: Supported by the Terahertz Multi User RF Transceiver System Development Project (Z211100004421012).

Biography: GONG Hang (1998-), male, Hubei, master degree, main research direction is the design of millimeter wave low-noise amplifier monolithic circuits and InP HEMT devices. Email: gonghang@ime.ac.cn

\*Corresponding authors: jinzhi@ime.ac.cn, suyongbo@ime.ac.cn

## Introduction

III-V compound semiconductors, represented by InP, have recently emerged as a technology of choice for Tera-Hz (THz) applications due to their low noise, low power consumption and high gain performance<sup>[1]</sup>. Northrop Grumman Space Technology first implemented the device with maximum oscillation frequency ( $f_{\max}$ ) exceeding 1THz in 2007<sup>[2]</sup>. In addition, their group successfully pushed the InP HEMT amplifier technology to 850 GHz for the first time in 2014<sup>[3]</sup>. Currently, the record for current-gain cutoff frequency ( $f_T$ ) is 750 GHz @ gate length ( $L_g$ ) = 20 nm<sup>[4]</sup> and  $f_{\max}$  is 1.5 THz @  $L_g$  = 25 nm<sup>[5]</sup>. Therefore, it is imperative to scale the physical gate length ( $L_g$ ) to improve the frequency response of the device. However, the  $L_g$  cannot be reduced indefinitely. According to delay-time analysis<sup>[6]</sup>, as the  $L_g$  decreases, the transit time under the gate  $\tau_{\text{text}}$  decreases sharply, resulting in a sharp increase in the proportion of extrinsic channel-charging delay  $\tau_{\text{ext}}$ . Therefore, reducing  $\tau_{\text{ext}}$  is another means to improve the device performance.

$\tau_{\text{ext}}$  is related to the parasitic resistance and parasitic capacitance. For the parasitic resistance, in addition to use multiple heavily doped cap layers<sup>[7,8]</sup>, it is to reduce the width of the gate recess to minimize parasitic series resistances, such as the source and drain resistance ( $R_s$  and  $R_D$ )<sup>[9]</sup>. The extrinsic capacitance can be decreased by increasing the spacing of gate recess or making a cavity structure<sup>[10]</sup>.

The gate recess process is the most critical process for InP HEMTs manufacturing, which has a significant impact on parasitic series resistances and capacitance. Dae-Hyun Kim *et al.* studied the effects of the side-recess spacing ( $L_{\text{side}}$ ), reporting that increasing  $L_{\text{side}}$  has a large impact on the subthreshold characteristics of the device due to a significant reduction of the gate leakage current and an improvement in its electrostatic integrity<sup>[11]</sup>. Both M. Samnoun *et al.*<sup>[12]</sup> and Keisuke Shinohara *et al.*<sup>[13]</sup> investigated the asymmetric gate recess technology, reporting that increase of the drain side recess ( $L_{\text{RD}}$ ) improves the  $f_{\max}$  due to the reduction of output conductance  $g_{\text{ds}}$  and capacitance  $C_{\text{gd}}$ . In addition, Tetsuya Suemitsu *et al.*<sup>[14]</sup> and Tae-Woo Kim *et al.*<sup>[15]</sup> developed a two-step-recessed gate process that improves high-speed performance.

However, seldom people have studied the impact of the asymmetric gate recess technology on two-step-recessed gate process. Therefore, it is imperative to carefully investigate the impact of the whole small recess offset in a double-recessed gate process on improving the high-frequency characteristics of InP HEMTs.

## 1 Process Technology

Table 1 shows the Gas Source Molecular Beam Epitaxy (GSMBE)-grown epitaxial layer structure on 3 inch semi-insulating InP (100) substrates that is used in this paper. In order to suppress the kink effect, the channel features a lattice-matched  $\text{In}_x\text{Ga}_{1-x}\text{As}$  with an indium content of 53%. In addition, a multi-layer cap structure that

combines a heavily Si-doped multi-layer cap ( $\text{In}_{0.65}\text{Ga}_{0.35}\text{As}/\text{In}_{0.53}\text{Ga}_{0.47}\text{As}/\text{In}_{0.52}\text{Al}_{0.48}\text{As}$ ) were used to minimize a tunneling resistance associated with the barrier layer between the cap and channel layer. The concentration of Si-doping to a multi-layer cap is  $3.0 \times 10^{19}$ ,  $1.0 \times 10^{19}$ , and  $1.0 \times 10^{19} \text{ cm}^{-2}$  respectively. The 4-nm InP layer acts as an effective gate recess etch-stopper. Hall measurements were carried out at room temperature, showing the carrier mobility of over 10 000  $\text{cm}^2/(\text{Vs})$  and the two-dimensional (2-DEG) sheet density of  $3.26 \times 10^{12} \text{ cm}^{-2}$ .

**Table 1 Epitaxial layer structures of the InGaAs HEMTs that are fabricated in this paper.**

**表 1 本文所做的 InGaAs HEMT 的外延层结构。**

N++ Cap	InGaAs, $x = 0.65$	10 nm
N+ Cap	InAlAs, $x = 0.53$	15 nm
N+ Cap	InAlAs, $x = 0.52$	15 nm
Stopper	InP	4 nm
Barrier	InAlAs, $x = 0.52$	8 nm
$\delta$ -doping	Si	-
Spacing	InAlAs, $x = 0.52$	3 nm
Channel	InGaAs, $x = 0.53$	15 nm
Buffer	InAlAs, $x = 0.52$	500 nm
3 Inch Semi-insulating InP (100) Substrate		

In order to avoid the degradation of the epitaxial structure by high temperature, the temperature of wafer in the whole fabrication process is lower than 300 °C. Similar to our previous work<sup>[16]</sup>, mesa isolation is achieved by using multiple acids to successively etch the epitaxial layer to the buffer layer. After device isolation, source-drain metal electrodes are formed by Ti/Pt/Au (15 nm/15 nm/50 nm) with thermal annealing. The distance between source and drain electrode was designed to be 2.4  $\mu\text{m}$ . The double-recessed gate process used to fabricate the T-shaped gates was as follows. Firstly, a  $\text{SiO}_2$  thin film was deposited by plasma-enhanced chemical vapor deposition (PECVD) to improve adherence of photoresist. And the opening size of the  $\text{SiO}_2$  mask was used to control the width of large gate recess. Next, the  $\text{SiO}_2$  mask was etched by reactive ion etching (RIE) using  $\text{CF}_4$  plasma after defining the gate-recess region by electronic beam lithography (EBL). After RIE, the InGaAs cap layer was removed by a mix solution of citric acid ( $\text{C}_6\text{H}_8\text{O}_7$ ) and hydrogen peroxide ( $\text{H}_2\text{O}_2$ ) to form the large gate recess, where it was measured about 500 nm.

To obtain a small gate recess, a e-beam gate process was developed, which is shown in Table. 1. The PMMA/Al/UVIII e-beam stack layers were used to define the gate and small gate recess. In order to avoid the miscible of the two photoresist layers, the metal Al layer is used for isolation, and it is easily soluble in alkaline developer. The top UVIII resist was exposed by a small dose and wide line. After that, the gate head was determined by TMAH development and rinsed in DI water. Subsequently, the gate foot was defined on a single layer of PMMA resist and was exposed by a big dose and narrow line.

The InAlAs cap layers were etched by  $H_3PO_4$ -solution down to the InP layer acting as an etch-stopped layer, where the small recess was measured about 100 nm. After the formation of the small recess, Ti/Pt/Au (3 nm/25 nm/350 nm) metals were evaporated and lifted off to form the T-shaped gate. The length of gate foot was 80 nm, and the gate stem was adjusted to be 250 nm to alleviate parasitic capacitances.

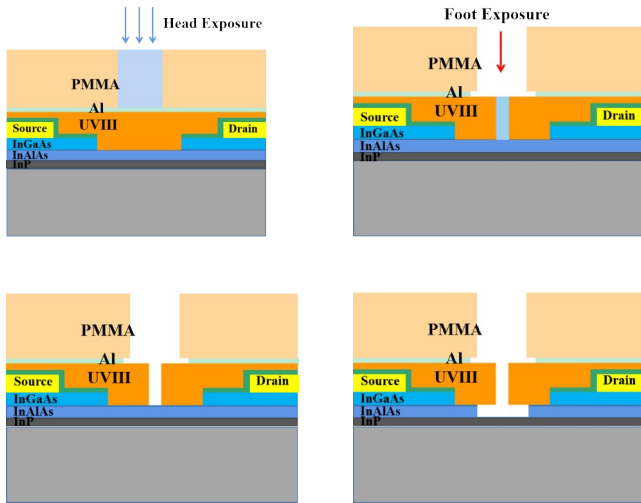


Fig. 1 The EBL process for T-gate fabrication and small gate recess (The layers below the InP etch-stopped layer are not shown)  
图1 用于T栅极制造和小栅极凹槽的EBL工艺(未显示InP蚀刻停止层下方的层)

The whole small recess could be located at the large recess center, or with an offset toward source/drain, where the position of gate metals was in the middle of the small recess. The offsets from large recess center were 0.0  $\mu\text{m}$  (type A), -0.1  $\mu\text{m}$  (type B), and +0.1  $\mu\text{m}$  (type C).

Finally, these devices were covered with a 20-nm-thick  $Si_3N_4$  dielectric film by PECVD (280  $^{\circ}\text{C}$ ). The SEM image of the cross section of the fabricated device is shown in Fig. 1, which is the whole small recess toward source.

## 2 DC & Microwave Characteristics

DC characteristics of devices were measured by an HP4142 semiconductor parameter analyzer. Figure 3 (a) shows the typical output characteristics of the InP-based InGaAs/InAlAs HEMTs with 80-nm gate length and  $50 \mu\text{m} \times 2$  gate width. These devices exhibit good pinchoff and excellent current saturation characteristics up to  $V_{DS} = 1.2 \text{ V}$ . The type A device exhibits a better drain current driving capability ( $I_{D,max}$ ). These devices exhibit the almost same ON-resistance ( $R_{ON}$ ), which is about  $0.70 \Omega \cdot \text{mm}$ . This is because the ohmic contact and access resistance components are the same during the whole small recess offset. The drain and source resistances ( $R_D$  and  $R_S$ ) are estimated from dc-measurements

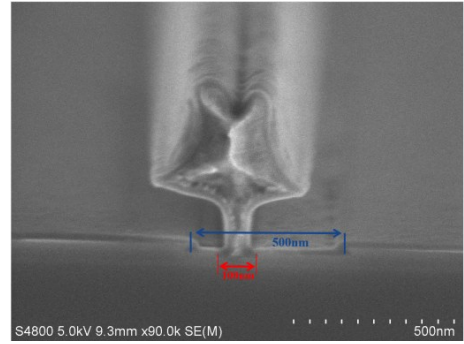


Fig. 2 SEM image of the cross section of the fabricated device with the whole small recess toward source (type B), where the large gate recess was measured about 500 nm and the small recess was measured about 100 nm

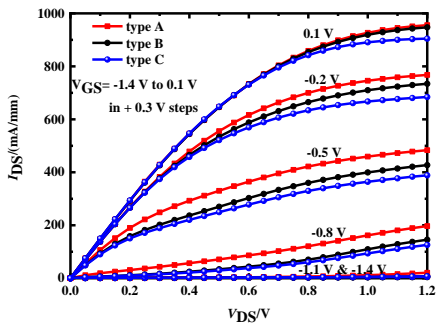
图2 所制造器件横截面的SEM图像,整个小凹槽朝向源极(B型),其中大栅极凹槽测量值约为500 nm,小凹槽测量值约为100 nm

( $R_S + R_D \approx 0.546 \Omega \cdot \text{mm}$ ), it can be also extracted from small signal equivalent circuit (SSEC) using a cold FET method [16].

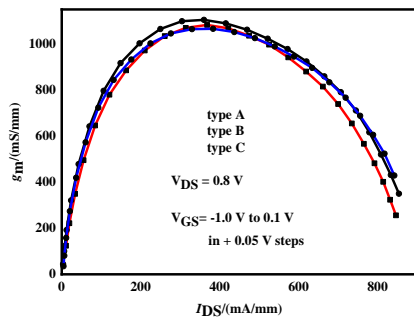
Figure 3 (b) shows the measured transconductance ( $g_m$ ) of the  $L_g = 80 \text{ nm}$  devices as a function of  $I_{DS}$  at a drain bias of 0.8 V. As the  $I_{DS}$  increases, the  $g_m$  increases firstly up to the  $g_{m,max}$  and then decreases gradually. The type B device with the whole small recess toward source exhibits the largest  $g_{m,max}$ , which is 1105 mS/mm. The best characteristic arises from the smaller  $R_S$ .

Figure 4 shows the dependence of the DC drain conductance ( $g_{ds,dc}$ ) on applied  $V_{DS}$ . The  $V_{GS}$  takes the voltage value corresponding to the  $g_{m,max}$ . When  $V_{DS}$  increases, the  $g_{ds,dc}$  of these devices decreases sharply at first and then decreases slowly. When  $V_{DS}$  is greater than 0.6 V, the  $g_{ds,dc}$  of type C always keeps a trend of being less than that of type A and type B. Because  $g_{ds,dc}$  is obtained from  $\partial I_{DS} / \partial V_{DS}$  and  $g_{ds}$  is obtained from  $\text{Re}(Y_{22})$  in the S-parameters,  $g_{ds}$  and  $g_{ds,dc}$  are related, which is consistent with the result of the parameters extraction below. From Equation (2), a smaller  $g_{ds}$  will contribute to improving the  $f_{max}$ .

The microwave characteristics of our representative  $L_g = 80 \text{ nm}$   $\text{In}_{0.53}\text{Ga}_{0.47}\text{As}/\text{In}_{0.52}\text{Al}_{0.48}\text{As}$  HEMTs are characterized from 0.1 to 50 GHz, using an Agilent precision network analyzer (PNA) system with off-wafer calibration. Pad parasitics are subtracted from the measured S-parameters using on-wafer OPEN and SHORT pads with identical geometry to the device pads. Figure 5 shows measured (symbols) and small-signal modeled (solid lines)  $H_{21}$ , MAG/MSG, and U versus frequency for these devices with the whole small recess offset. Using the de-embedded S-parameters, we build a conventional small-signal model, based on our previous research [17]. The bias condition is at  $V_{DS} = 0.8 \text{ V}$ . And  $V_{GS}$  takes the voltage value corresponding to the  $g_{m,max}$ . From the de-embedded S-parameters, the values of  $f_T$  could be obtain by extrapolating  $H_{21}$  with a slope of -20 dB/decade and the values of  $f_{max}$  are estimated from the small signal model. It is good that such a combination of  $f_T = 372 \text{ GHz}$  and  $f_{max} = 394$



(a)



(b)

Fig. 3 Partial DC and RF characteristics of InP HEMT: (a) DC characteristics of the InGaAs/InAlAs HEMTs with the whole small recess offset, and (b) the measured transconductance ( $g_m$ ) of the devices as a function of  $I_{DS}$ , for the value of  $V_{DS} = 0.8$  V ( $L_g = 80$  nm,  $W_g = 50 \mu\text{m} \times 2$ )

图3 InP HEMT的部分直流以及射频特性:(a)具有整个小凹槽偏移的InGaAs/InAlAs HEMT的直流特性,以及(b)测量到的器件跨导( $g_m$ )作为IDS的函数,其中 $V_{DS} = 0.8$  V ( $L_g = 80$  nm,  $W_g = 50 \mu\text{m} \times 2$ )

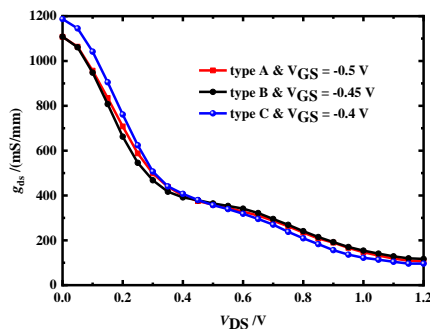
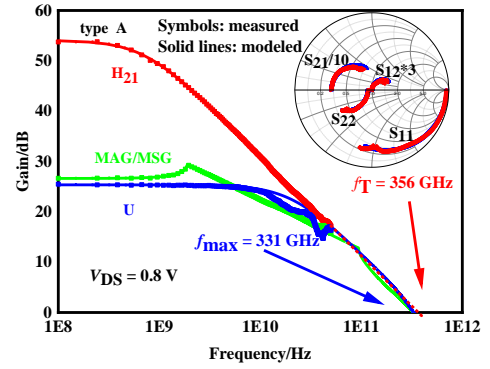


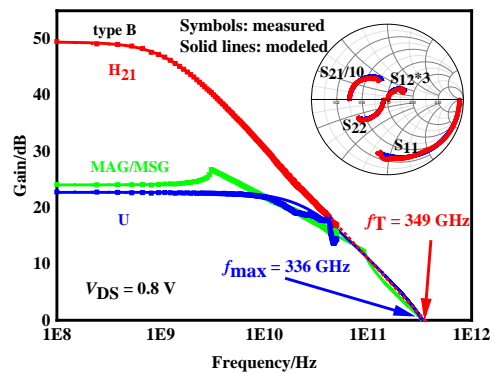
Fig. 4 Dependence of DC drain conductance on applied  $V_{DS}$  with different structures

图4 不同结构的直流漏极电导对所加  $V_{DS}$  值的变化

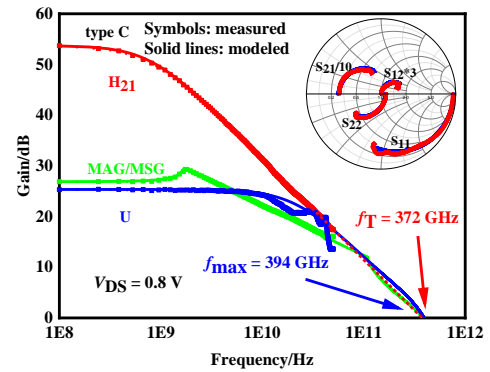
GHz is demonstrated from the type C device with the whole small recess toward drain, at a relatively small value of  $V_{DS} = 0.8$  V and  $V_{GS} = -0.4$  V.



(a)



(b)



(c)

Fig. 5 Measured (symbols) and small-signal modeled (lines) RF gains [ $|h_{21}|$ , U and maximum available gain (MAG/MSG)] versus frequency with the  $L_g = 80$  nm InGaAs/InAlAs HEMTs. The offsets from large recess center were  $0.0 \mu\text{m}$  (type A),  $-0.1 \mu\text{m}$  (type B), and  $+0.1 \mu\text{m}$  (type C). The bias conditions were near the  $g_m$  peak gate voltage and at  $V_{DS} = 0.8$  V

图5 使用  $L_g = 80$  nm InGaAs/InAlAs HEMT测量的和小信号建模RF增益 [ $|h_{21}|$ , U和最大可用增益 (MAG/MSG)]与频率的关系。距大凹槽中心的偏移量为  $0.0 \mu\text{m}$  (A型)、 $-0.1 \mu\text{m}$  (B型)和  $+0.1 \mu\text{m}$  (C型)。偏置条件接近  $g_m$  峰值栅极电压且  $V_{DS} = 0.8$  V

Figure 6 plots the extracted  $f_T$  as a function of  $I_{DS}$  for these devices at  $V_{DS} = 0.8$  V, which consists with the  $g_m$

against  $I_{DS}$  in Fig. 3(b). The type C device have the largest  $f_T$  of all  $f_T - I_{DS}$  characteristics. At an  $I_{DS}$  of approximately 100 mA/mm which is a typical choice of the bias condition for most of the LNA designs, the type C device displays  $f_T$  over 275 GHz.

The  $f_T$  and  $f_{max}$  can be expressed as :

$$f_T = \frac{g_{mi}}{2\pi \{ (C_{gs} + C_{gd}) [1 + g_{ds} (R_s + R_d)] + C_{gd} g_{mi} (R_s + R_d) \}}, \quad (1)$$

$$f_{max} = \frac{f_T}{\sqrt{4g_{ds} (R_g + R_i + R_s) + \frac{2C_{gd}}{C_{gs}} \left( \frac{C_{gd}}{C_{gs}} + g_{mi} (R_i + R_s) \right)}}. \quad (2)$$

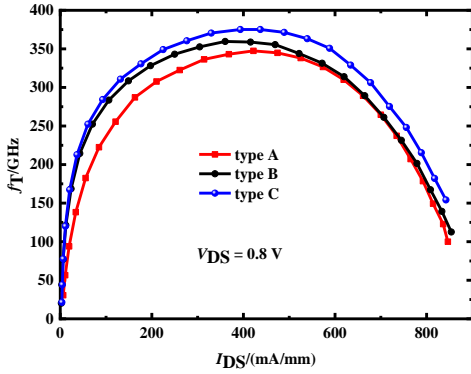


Fig. 6 Extracted  $f_T$  against  $I_{DS}$  of  $L_g = 80$  nm InGaAs/InAlAs HEMTs at  $V_{DS} = 0.8$  V with different structures

图6 不同结构的  $L_g = 80$  nm InGaAs/InAlAs HEMT 在  $V_{DS} = 0.8$  V 下针对  $I_{DS}$  提取的  $f_T$

Table 2 shows the small-signal modeling parameters for different structures, including  $R_s$ ,  $R_D$ ,  $g_{mi}$ ,  $C_{gs}$ ,  $C_{gd}$ , and  $g_{ds}$ . Compared with type A and type B, type C has the smallest capacitance  $C_{gs}$ . This is because the type C device with the whole small recess toward drain results in smaller extrinsic capacitance. At the same time, according to Table 2 and Fig. 4 shows that the type C has the smallest  $g_{ds}$ . Although the  $g_{mi}$  of type C is the smallest, the parasitic resistance of the three devices is almost the same, and combined with the influence of other parameters, the type C finally obtains the largest  $f_T$ . In terms of  $f_{max}$ , it depends on the combined influence of several parameters. The type C device obtains the largest  $f_{max}$  due to the small  $g_{ds}$  and large  $f_T$ . Therefore, it should be finally emphasized that the device with the whole small recess toward drain in a double-recessed gate process could improve the high-frequency characteristics.

### 3 Conclusion

In summary, we experimentally investigate the impact of the whole small recess offset on the lattice-matched InP-based HEMTs in a double-recessed gate process, where  $L_g = 80$  nm. These devices exhibit the same  $R_{ON}$ , and the device with the whole small recess toward source has the largest  $g_{m,max}$  due to a smaller  $R_s$ . For RF responses of these devices, the device with the whole small recess toward drain achieves an excellent characteristic of  $f_T = 372$  GHz, and  $f_{max} = 394$  GHz. In the following research, the  $g_m$  of the device will be further im-

Table 2 Small-signal model parameters of the  $L_g = 80$  nm InGaAs/InAlAs HEMTs at  $V_{DS} = 0.8$  V, with different structures.

表2 不同结构的  $L_g = 80$  nm InGaAs/InAlAs HEMT 在  $V_{DS} = 0.8$  V 时的小信号模型参数。

Symbol	Type A	Type B	Type C
$V_{GS}$ [V]	-0.50	-0.45	-0.40
$C_{gs}$ [fF/mm]	418	432	388
$C_{gd}$ [fF/mm]	103	97	99
$R_s$ [ $\Omega \cdot \text{mm}$ ]	0.159	0.149	0.169
$R_D$ [ $\Omega \cdot \text{mm}$ ]	0.387	0.397	0.377
$g_{ds}$ [mS/mm]	305.5	304.5	240
$g_{mi}$ [mS/mm]	1513	1566	1487
$f_{T,max}$ [GHz]	356	349	372
$f_{max,model}$ [GHz]	331	336	394

Table 3 Related device performance comparison

表3 相关器件性能对比

$L_g$ (nm)	$g_{m,max}$ (mS/mm)	$f_T$ (GHz)	$f_{max}$ (GHz)	Time	Ref
75	1 950	270	910	2017	[19]
100	1 700	300	700	2022	[20]
70	1 600	310	540	2014	[21]
75	1 331	260	800	2021	[12]

proved to increase the  $f_T$  by using a channel with Indium-rich composition.

### 4 Acknowledgement

This work was supported by Development of Terahertz Multi-user RF Transceiver System (Grant No. Z211100004421012). The authors would like to thank Yan-kui Li for his assistance during the measurements. We thank Engineer Feng Yang for his discussion on the process and Professor Ding Peng for his guidance.

### References

- [1] Kim D and Alamo J. 30-nm InAs PHEMTs With  $f_T = 644$  GHz and  $f_{max} = 681$  GHz [J]. *IEEE Electron Device Letters*, 2010, **31**(8): 806-808.
- [2] Lai R, Mei X B, Deal W R, *et al.* Sub 50 nm InP HEMT Device with  $f_{max}$  Greater than 1 THz [C]. 2007 IEEE International Electron Devices Meeting (IEDM), 2007: 609-611.
- [3] Deal W R, Leong K, A. Zamora, Radisic V, *et al.* Recent progress in scaling InP HEMT TMIC technology to 850 GHz [C]. 2014 IEEE MTT-S International Microwave Symposium (IMS2014), **2014**: 1-3.
- [4] Park W, Jo H, Kim H, *et al.* Terahertz  $\text{In}_{0.8}\text{Ga}_{0.2}\text{As}$  quantum-well HEMTs toward 6G applications [C]. 2022 International Electron Devices Meeting (IEDM), 2022: 11.4.1 - 11.4.4.
- [5] Mei X B, Yoshida W, Lange M, *et al.* First Demonstration of Amplification at 1 THz Using 25-nm InP High Electron Mobility Transistor Process [J]. *IEEE Electron Device Letters*, 2015, **36**(4): 327-329.
- [6] Jo H, Yun S, Kim J, *et al.* Sub-30-nm  $\text{In}_{0.8}\text{Ga}_{0.2}\text{As}$  Composite-Channel High-Electron-Mobility Transistors With Record High-Frequency Characteristics [J]. *IEEE Transactions on Electron Devices*, 2021, **68**(4): 2010-2016.
- [7] Chen K J, Enoki T, Maezawa K, *et al.* High-performance InP-based enhancement-mode HEMTs using non-alloyed ohmic contacts and Pt-based buried-gate technologies [J]. *IEEE Transactions on Electron Devices*, 1996, **43**(2): 252-257.
- [8] Shinohara K, Yamashita Y, Endoh A, *et al.* 547 GHz  $f_T$   $\text{In}_{0.7}\text{Ga}_{0.3}\text{As}-\text{In}_{0.52}\text{Al}_{0.48}\text{As}$  HEMTs with reduced source and drain resistance [J]. *IEEE Electron Device Letters*, 2004, **25**(5): 241-243.

- [9] Feng Ruize, Wang Bo, Cao Shurui, *et al.* Impact of symmetric gate-recess length on the DC and RF characteristics of InP HEMTs [J]. *Chinese Physics B*, 2022, **31**(1): 018505.
- [10] Takahashi T, Makiyama K, Hara N, *et al.* Improvement in high frequency and noise characteristics of InP-based HEMTs by reducing parasitic capacitance [C]. 2008 20th International Conference on Indium Phosphide and Related Materials(ICIPRM), 2008: 1-4.
- [11] Kim D, Alamo J, Lee J, *et al.* The Impact of Side-Recess Spacing on the Logic Performance of 50 nm InGaAs HEMTs [C]. 2006 International Conference on Indium Phosphide and Related Materials Conference Proceedings, Princeton(ICIPRM), 2006: 177-180.
- [12] Samnoui M, Wichmann N, Wallart X, *et al.* 75 nm Gate Length PHEMT With  $f_{\max} = 800$  GHz Using Asymmetric Gate Recess: RF and Noise Investigation [J]. *IEEE Transactions on Electron Devices*, 2021, **68**(9): 4289-4295.
- [13] Shinohara K, Chen P S, Bergman J, *et al.* Ultra-High-Speed Low-Noise InP-HEMT Technology [C]. 2006 IEEE MTT-S International Microwave Symposium Digest(MWSYM), 2006: 337-340.
- [14] Suemitsu T, Yokoyama H, Umeda Y, *et al.* High-performance 0.1- $\mu\text{m}$ -gate enhancement-mode InAlAs/InGaAs HEMT's using two-step-recessed gate technology [J]. *IEEE Transactions on Electron Devices*, 1999, **46**(6): 1074-1080.
- [15] Kim T, Kim D, Park S, *et al.* A Two-Step-Recess Process Based on Atomic-Layer Etching for High-Performance  $\text{In}_{0.52}\text{Al}_{0.48}\text{As}/\text{In}_{0.53}\text{Ga}_{0.47}\text{As}$  p-HEMTs [J]. *IEEE Transactions on Electron Devices*, 2008, **55**(7): 1577-1584.
- [16] Ding Peng, Chen Chen, Ding Wuchang, *et al.* Ultra-thin 20 nm-PECVD- $\text{Si}_3\text{N}_4$  surface passivation in T-shaped gate InAlAs/InGaAs InP-based HEMTs and its impact on DC and RF performance [J]. *Solid-State Electronics*, 2016, **123**: 1-5.
- [17] Dambrine G, Cappy A, Heliodore F, *et al.* A new method for determining the FET small-signal equivalent circuit [J]. *IEEE Transactions on Microwave Theory and Techniques*, 1988, **36**(7): 1151-1159.
- [18] Asif M, Peng D, Chen C, *et al.* Analysis of Passivation Techniques in InP HEMTs and Implementation of an Analytical Model of  $f_T$  Based on the Small Signal Equivalent Circuit [J]. *Journal of Nanoscience and Nanotechnology*, 2019, **19**(5): 2537-2546.
- [19] Takahashi T, Kawano Y, Makiyama K, *et al.* Enhancement of  $f_{\max}$  to 910 GHz by Adopting Asymmetric Gate Recess and Double-Side-Doped Structure in 75-nm-Gate InAlAs/InGaAs HEMTs [J]. *IEEE Transactions on Electron Devices*, 2017, **64**(1): 89-95.
- [20] Zhou Guo, Bi Yingsheng, Chen Zhuo, *et al.* Preparation and Performances of InP HEMT Device with Cavity Gate Structure [J]. *Semiconductor Technology*, (周国, 毕胜赢, 陈卓, *et al.* InP HEMT 空腔栅结构器件制备及性能 [J]. *半导体技术*), 2022, **47**(06): 443-447.
- [21] Zhang Lisen, Feng Zhihong, Xing Dong, *et al.* 70 nm gate-length THz InP-based  $\text{In}_{0.7}\text{Ga}_{0.3}\text{As}/\text{In}_{0.52}\text{Al}_{0.48}\text{As}$  HEMT with  $f_{\max}$  of 540 GHz [C]. 2014 XXXIth URSI General Assembly and Scientific Symposium (URSI GASS). 2014: 1-4.